The Cryosphere Discuss., 3, 1069–1107, 2009
www.the-cryosphere-discuss.net/3/1069/2009/

The Cryosphere Discussions

This discussion paper is/has been under review for the journal The Cryosphere (TC).
Please refer to the corresponding final paper in TC if available.

Surface melt magnitude retrieval over Ross Ice Shelf, Antarctica using coupled MODIS near-IR and thermal satellite measurements

D. J. Lampkin[1] **and C. C. Karmosky**[2]

[1]Department of Geography, Department of Geosciences, Penn State University, University Park, Pennsylvania, USA
[2]Department of Geography, Penn State University, University Park, Pennsylvania, USA

Received: 4 September 2009 – Accepted: 14 October 2009 – Published: 2 December 2009

Correspondence to: D. J. Lampkin (djl22@psu.edu)

Published by Copernicus Publications on behalf of the European Geosciences Union.

Abstract

Surface melt has been increasing over recent years, especially over the Antarctic Peninsula, contributing to disintegration of shelves such as Larsen. Unfortunately, we are not realistically able to quantify surface snowmelt from ground-based methods because there is sparse coverage of automatic weather stations. Satellite based assessments of melt from passive microwave systems are limited in that they only provide an indication of melt occurrence and have coarse spatial resolution. An algorithm was developed to retrieve surface melt magnitude using coupled near-IR/thermal surface measurements from MODIS were calibrated by estimates of liquid water fraction (LWF) in the upper 1 cm of the firn derived from a one-dimensional physical snowmelt model (SNTHERM89). For the modeling phase of this study, SNTHERM89 was forced by hourly meteorological data from automatic weather station data at reference sites spanning a range of melt conditions across the Ross Ice Shelf during a relatively intense melt season (2002). Effective melt magnitude or $LWF_{<eff>}$ were derived for satellite composite periods covering the Antarctic summer months at a 4 km resolution over the entire Ross Ice Shelf, ranging from 0–0.5% $LWF_{<eff>}$ in early December to areas along the coast with as much as 1% $LWF_{<eff>}$ during the time of peak surface melt. Spatial and temporal variations in the magnitude of surface melt are related to both katabatic wind strength and advection during onshore flow.

1 Introduction

Recent dramatic disintegration of the Larsen B Ice Shelf in 2002 and the partial collapse of the Wilkins Ice Shelf in 2008 and 2009 have prompted the urgent need to understand ice shelf dynamics. Results from models have suggested that collapsing ice shelves on the West Antarctic Ice Sheet (WAIS) are not a completely new phenomenon, as sporadic collapse and re-growth has occurred several times over the past million years (MacAyeal, 1992). However, the collapse of large Antarctic ice shelves

TCD
3, 1069–1107, 2009

has the potential to increase sea level in the near-term significantly beyond anything experienced over the course of human history. The collapse of Larsen B is known to have accelerated the flow rate of surrounding feeder glaciers by as much as 600% (Scambos et al., 2004). This acceleration increases the amount of ice flowing into the Southern Ocean, directly contributing to sea-level rise. Surface melt on Larsen B has been shown to not only have been substantial during the 2001–2002 melt season (Sergienko and MacAyeal, 2005) but also one of the primary causes of its collapse (van den Broeke, 2005). Surface melt water can infiltrate into crevasses on the ice shelf surface, enhancing further fracturing when a crevasse is more than 90% inundated with melt-water (Scambos et al., 2000). Because surface melt has a significant impact on ice shelf stability, a retrieval of surface melt water fraction beyond the assessment of melt occurrence currently derived from passive microwave approaches (e.g. Ridley, 1993; Abdalati and Steffen, 1995; Tedesco, 2007) or microwave scatterometry (e.g. Nghiem et al., 2001; Steffen et al., 2004) would be beneficial. A broader evaluation of the spatio-temporal variability of surface melt over all Antarctic ice shelves would improve our ability to assess how changes in climate affect ice shelf stability.

2 Background

The dramatic response of an ice shelf to atmospheric warming has been most exemplified along the Antarctic Peninsula (AP), which has experienced "extreme climate variability" and "significant warming" of up to 0.56°C per decade (King et al., 2002; Turner et al., 2005). Doake and Vaughan (1991) used remotely-sensed imagery in the visible spectrum to detect retreat in the Wordie Ice Shelf on the AP and found strong correlations with long-term increases in atmospheric temperature across the region. Turner et al. (2005) also noted a long-term decrease in sea ice concentration in the Antarctic Peninsula region, but found that temperature trends across most of Antarctica (with the exception of the Peninsula) are insignificant. More recently, however, Steig et al. (2009) determined that increasing temperatures are statistically significant

TCD
3, 1069–1107, 2009

when aggregated to a regional scale. While some ambiguity exists regarding positive temperature trends in the interior of Antarctica, it is clear that areas along the Antarctic Peninsula and the coastal areas of West Antarctica are experiencing large increases in surface air temperature, and ice shelves here are becoming more vulnerable to surface melt and collapse. This study will outline an empirical method for quantifying the effective amount of liquid water fraction ($LWF_{<eff>}$) in the upper layers of the firn. This method relies on changes in the bulk crystal size of the firn as melt is occurring, which is detected via: 1) the relationship between optical grain size and near-infrared reflectance and 2) the relationship surface skin temperature and melt conditions.

Previous studies addressing the issue of surface melt have focused on the use of passive and active microwave data to detect the presence of melt. The Special Sensor Microwave Radiometer (SMMR) and Special Sensor Microwave Imager (SSM/I) radiometers have long been used to assess surface melt conditions on both the Greenland and Antarctic Ice sheets (Jezek et al., 1994; Ridley, 1993; Zwally and Fiegles, 1994; Abdalati and Steffen, 1995; Mote and Anderson, 1995; Mote, 2007; and several others). The transition from dry to wet snow results in a rapid increase in microwave emissivity when surface scattering begins to dominate emissions over volume scattering (Mätzler and Hüppi, 1989). The Rayleigh-Jeans approximation for surface emitted radiation in the microwave part of the electromagnetic (EM) spectrum is measured by microwave radiometers measuring brightness temperature given by:

$$T_b(\lambda) \approx \varepsilon T_p \quad (1)$$

where T_b is the microwave brightness temperature at wavelength (λ), ε is emissivity, and T_p is the effective physical temperature (Zwally, 1977). Wet snow is a mixture of ice crystals, air, and liquid water. The dielectric constant for wet snow is a weighted average of the dielectric constant of each component (Mätzler et al., 1984). The dielectric constant for snow has both a real and imaginary component. As snowmelt begins to occur, the imaginary component of dielectric constant increases rapidly (Tiuri et al., 1984), resulting in a sharp increase in emissivity and consequently, an increase in microwave brightness temperatures. As snow begins to moisten, penetration depth

of the microwave radiation sharply decreases, and volume scattering is nearly absent, with wet snow behaving almost as a blackbody (Mätzler and Hüppi, 1989). This sharp change in brightness temperature quickly saturates at approximately 1% liquid water fraction, and prevents the quantitative assessment of surface melt fraction using microwave frequencies. One important passive microwave method for detecting surface melt conditions is the cross-polarized gradient ratio, or XPGR (Abdalati and Steffen, 1995). The XPGR is calculated as follows:

$$\mathrm{XPGR} = (T_B^{19\mathrm{H}} - T_B^{37\mathrm{V}})/(T_B^{19\mathrm{H}} + T_B^{37\mathrm{V}}) > A \quad (2)$$

where an XPGR value exceeding A (-0.0158 derived over Greenland) is designated as a melt event. The utilization of a ratio between two microwave frequencies allows for the effects of emissivity alone, rather than emissivity and temperature, to control the XPGR. As snow becomes wet, the differences in brightness temperatures between a vertically polarized signal and a horizontally polarized signal decreases. A higher XPGR would therefore indicate a melt event somewhere within the effective footprint of the microwave radiometer in excess of 1% liquid water fraction by volume. The maximum difference, and therefore the clearest ratio was noted between the 19 H and 37 V channels. The XPGR also combines the benefits of the strong relationship between surface melt and a horizontally-polarized passive microwave signal with the vertically-polarized signal which is not dependant on the spatial variability of surface temperature (Abdalati and Steffen, 1997). Fettweis et al. (2007) developed an improved XPGR melt algorithm to preserve continuity in the melt season during days where dense cloud cover containing liquid precipitation gave erroneous passive microwave measurements. However with the short duration of melt and the absence of liquid precipitation over the Ross Ice Shelf, the use of this methodology is not necessary for this study, and we chose to use the XPGR. Future work involving more temperate Antarctic ice shelves, such as Larsen, could benefit from the enhancements in the ImpXPGR.

In addition to the passive microwave imagery, scatterometers have been used to detect surface melt. While the QuikSCAT (QSCAT) scatterometer was developed to

measure surface winds over the ocean at a daily, 25-km resolution, it has proved useful in detecting surface melt of ice sheets due to a high sensitivity to the presence of liquid water in the snowpack. Increases in snow wetness result in the absorption of microwave radiation and consequently a decrease in backscatter of four times to more than an order of magnitude and verified based on surface temperature and radiation measurements from ground-based meteorological stations (Nghiem et al., 2001). Scatterometry is limited in that it cannot resolve absolute wetness of the snowpack as backscatter amounts depend not only on snow wetness but also on grain size. This effect is minimized by focusing on diurnal backscatter differences and assuming that the grain size does not change over the course of the day, and that diurnal backscatter changes are the result of a change in snow wetness

3 Study region

The Ross Ice Shelf (Fig. 1) spans an area along the Antarctic coast 165° W across the 180th meridian to 165° E. While the grounding line of Ross extends poleward to approximately 86° S, the majority of surface melt is typically confined to the warmest areas along the coastal ice shelf margin. Sea ice abuts the ice shelf front, which extends northward to 77° S at the westernmost corner, and 78° S on the eastern side. The Transantarctic Mountains border the western flank of the Ross Ice Shelf, while the Siple Coast is located along the eastern side. Several large ice streams feed the ice shelf from the Siple Coast side, while smaller, but still significant outlet glaciers through the Transantarctic range provide a path for ice and katabatic winds to flow onto the shelf from the East Antarctic Plateau.

4 Data

Data for this study included AWS wind speed, temperature, and relative humidity; NCEP/NCAR Reanalysis-derived radiation fluxes and precipitation, measured short-

TCD
3, 1069–1107, 2009

wave radiation, and MODIS near-IR and thermal imagery for the December 2002–January 2003 time period. Even though the Antarctic Peninsula has experienced the largest changes in surface temperatures, and has experienced some of the most significant effects of ice shelf surface melting, readily available Automated Weather Station (AWS) data over the AP is limited to only one point location (the Larsen AWS) for our study time period. Therefore, in order to create a robust empirical model for surface melt, data must be used from another location that has a denser network of weather stations. The Ross Ice Shelf serves as a location where there is some surface melt occurring during the peak of the summer season, but with an overall colder ambient temperature, and contains several weather stations with a continuous meteorological record over a substantially intense melt season.

4.1 AWS network

The National Science Foundation Office of Polar Programs Automatic Weather Station project (Stearns et al., 2009) is a network of weather stations across Antarctica that is used to support field forecasting and support as well as a range of climate studies. It is supported by the University of Wisconsin Antarctic Meteorological Research Center, with data available online. Several stations have data for the 2002/03 study season on Ross Ice shelf, allowing for a wide sampling of climate conditions. Five stations are used for the model calibration, including: Pegasus North, Pegasus South, Gill, Ferrell, and Laurie II. These sites have surface AWS instruments that record temperature, wind speed, and relative humidity as well as other climate variables. Data were obtained for each climate variable at 10-min intervals for all five stations. They were then manually quality-controlled and averaged to 6-hourly time-steps.

4.2 NCEP/NCAR reanalysis

NCEP/NCAR reanalysis (Kalnay et al., 1996) output is available online at a 2.5°×2.5°, 6-hourly resolution. Several meteorological variables were obtained for the reanalysis

gridpoint closest to each reference AWS site. From 6-hourly averaged precipitation rate estimates, 6-hourly precipitation totals were calculated. Downwelling shortwave, reflected shortwave, and downwelling longwave radiation fluxes were also obtained from the reanalysis dataset. Bromwich and Fogt (2004) indicate that ERA40 reanalysis is preferable to NCEP/NCAR reanalysis output for the middle and high latitudes of the southern hemisphere; however, ERA40 reanalysis has been compiled only through August, 2002. While other datasets have extended the ERA40 reanalysis beyond August 2002, specifically the RACMO dataset (Lipzig et al., 2001), NCEP/NCAR reanalysis provided a sufficient data source for this preliminary investigation. The quality of the NCEP/NCAR output has been shown to be better for the summer months and toward the latter part of the data record, when more satellite information was fed into the reanalysis algorithms. Despite the coarse resolution of the NCEP/NCAR reanalysis dataset, generally low precipitation amounts, and the insensitivity of our calibration procedute to precipitation forcing make these reanalysis output sufficient for our analysis.

4.3 NSF UV/Vis

While downwelling solar radiation data is available from the NCEP/NCAR reanalysis project, reported radiation values were found to create unrealistically high liquid water fractions at the reference stations, and were substantially larger than radiation fluxes measured at the ground in other locations. Measured radiation data from a ground source were necessary for SNTHERM89 forcing. Radiation data from McMurdo station was provided by the NSF UV Monitoring Network, operated by Biospherical Instruments Inc. under a contract from the United States National Science Foundation's Office of Polar Programs via Raytheon Polar Services Company. Average incoming shortwave measurements over the 290 nm to 600 nm wavelengths were averaged over 6-hourly time periods for the 2002/03 ablation season, then the values were doubled to provide an "upper-bound" estimate for incoming solar radiation over all UV and visible wavelengths. Shortwave radiation fluxes were substantially lower than those estimated

in the NCEP/NCAR reanalysis dataset, often by as much as 50% for some time periods. While this is perhaps correct to only within an order of magnitude, it was found that the liquid water fractions obtained using the coarsely gridded NCEP/NCAR radiation measurement were unreasonably high and inconsistent with passive microwave-derived melt occurrence. Reflected shortwave radiation was estimated by calculating the albedo from NCEP/NCAR reanalysis and applying that factor to the measured radiation from the NSF UV monitoring network. Because measured infrared radiation measurements were not available, it was necessary to use estimates from NCEP/NCAR reanalysis for this SNTHERM input.

4.4 Satellite data

MODIS data was obtained from the NASA Warehouse Inventory Search Tool (WIST). MODIS/Aqua Surface Reflectance 8-Day L3 Global 500 m SIN Grid V004 and MODIS/Aqua Sea Ice Extent and Ice Surface Temperature Daily L3 Global 4 km Ease-Grid Day V005 imagery (Hall et al., 2007), products MYD09A1and MYD29E1, respectively, were used in this study. Infrared reflectance was obtained via MODIS band 5 (1230–1250 nm), a region of the electromagnetic spectrum where reflectance is known to be highly dependent on snow grain size, and therefore surface melt history. Unfortunately, because cloud cover is opaque to infrared radiation, it is impossible for the satellite to detect infrared reflection and surface temperature values unless a clear sky is present. Therefore, a cloud mask is applied to the MODIS imagery pre-processing, significantly reducing the temporal frequency of the available satellite imagery. To reduce the number of data gaps caused by this effect, 8-day composite imagery was necessary, as most areas are imaged at least once in this time period. Version 5 data is currently unavailable for infrared reflectance for this time period and study area. Because 8-day composite imagery is unavailable for ice shelf surface temperature it was necessary to manually composite the thermal imagery to the same 8-day periods as the reflectance imagery. MYD29E1 were composited from the daily 4 km LST product and stored on a 4 km grid as the average values of clear-sky LST during an 8-day pe-

riod. While 1 km resolution ice surface temperature is available from the NSIDC, this data has significant gaps across the 180° meridian, which crosses through the middle of the study area, so the more spatially contiguous 4 km resolution imagery was used.

Passive microwave brightness temperatures (Cavalieri et al., 2004) were obtained for XPGR validation. Ascending and Descending 19 H and 37 V polarizations were used to obtain a daily averaged XPGR for the Ross Ice Shelf and vicinity (Abdalati and Steffen, 1995, 2007). These data are available online from the NSIDC.

5 Methods

Snow is a selective absorber in the near-infrared portion of the electromagnetic spectrum, with albedo ranging from near-complete reflectance to near-complete absorbance over the solar spectrum (Nolin and Dozier, 2000). While the bulk optical properties of ice and water are similar, reflectance and transmittance is largely dependent on variations in the complex refractive index of the ice, where specifically absorption is due to variations in the imaginary part of the complex refractive index of ice (Dozier, 1989). The absorption coefficient varies substantially in the wavelengths from 0.4 to 2.4 μm (Dozier, 1989). Several have examined the strong relationship between snow spectral reflectance and grain-size, and modeled snow reflectance from the optical properties of snow and ice (Bohren and Barkstrom, 1974; Wiscombe and Warren, 1981; Nolin and Dozier, 2000; Painter et al., 2003). Changes in snow reflectance in the near-infrared (NIR) and shortwave infrared (SWIR) of the electromagnetic spectrum are strongly dependent on changes in optical grain size (Wiscombe and Warren, 1980), with an inverse relationship between albedo and grain size. This relationship is strongest at 1.03 μm and 1.26 μm where the difference in reflectance between small and large grains is most substantial (Hyvärinen and Lammasniemi, 1987; Nolin and Dozier, 2000). As grain size increases, optical depth in the near infrared decreases (from 3 cm to about 0.5 cm), assuming constant snowpack density (Nolin and Dozier, 2000). In wet snow with high liquid water content, heat flow from large grains causes

smaller particles, which are at lower temperature, to melt and merge into larger clusters (Colbeck, 1982, 1989). As bulk grain cluster radius increases, an incident photon will have a high probability of being scattered when it traverses the air-ice interface, but a greater chance of absorption while passing through the ice grain (Warren, 1982). Grain clusters optically behave as single grains, increasing the mean photon path length, subsequently increasing the opportunity for absorption and reduction in reflectance. Larger grains increase the degree of absorption, particularly in the shortwave infrared region, causing a substantial reduction in reflectance. The maximum sensitivity of reflectance to changes in grain size is in the shortwave (SWIR) region of the EM spectrum at approximately 1.1 μm (Nolin and Dozier, 2000). Because shortwave infrared reflectance is known to be proportional to grain size, which in turn is partially dependent on the degree of melting that has occurred, it can be used as a proxy for quantifying the amount of surface melt present in the snowpack (Lampkin and Yool, 2004; Peng, 2007; Lampkin and Peng, 2008). The use of snow surface reflectance alone to track the surface melt process is not sufficient, because substantial decreases in reflectance are not due solely to grain enlargement associated with entrained liquid water. For example, small amounts of absorbing impurities can also reduce snow reflectance in the visible wavelengths (Warren and Wiscombe, 1981; Grenfell et al., 1981; Bohren, 1986). In this case, surface temperature can be used as a plausible mechanism in isolating the component in reduced reflectance that is due to the melt process.

Snow thermal emission (8–14 μm wavelengths) is a function of snow surface skin temperature and emissivity (Marks and Dozier, 1992). Snow surface temperature information coupled with near-IR information can assist in refining the assessment of melt magnitude from surface reflectance. Surface melt is physically driven by increases in temperature above freezing, and higher temperatures can therefore be correlated to areas where more surface melt is occurring. Lampkin and Yool (2004) employed visible, near infrared, and thermal wavelength for the creation of a near-surface moisture index (NSMI) which provided a categorical determination of snow wetness in alpine areas, but not providing quantitative estimates for liquid water fraction. This index relied

on the decreased visible and infrared albedo as melting and grain size increased.

Lampkin and Peng (2008) have demonstrated the feasibility of surface liquid water fraction ($LWF_{<eff>}$) retrieval through calibrating satellite-derived near-IR/thermal signatures with a physical snowmelt model (SNTHERM89) forced by meteorological data collected from GC-Net stations on the western portion of the Greenland Ice Sheet. This empirical retrieval has been designated as effective melt magnitude (E-melt) primarily because it represents a measure of temporally integrated liquid water fraction over an 8-day period at 1 km^2 within the upper 5 cm of the glacial firn at a relative accuracy of ~±2%, rather than an instantaneous measurement of surface liquid water faction at a point location. We propose using a similar method for detecting and quantifying surface melt on Antarctic ice shelves using coupled near-IR and thermal signatures from Moderate Resolution Imaging Spectroradiometer (MODIS) satellite data.

In this study, MODIS LST was processed at a 4 km scale over Antarctic ice shelves, giving the coupled near-IR/thermal retrieval model an effective 4 km resolution over the Ross Ice Shelf. MODIS LST and atmospherically corrected shortwave Infrared (SWIR) surface reflectance grids were acquired over an analysis period spanning from December through January, during the 2002/03 Antarctic ablation season. Cloud cover is a major limitation when using data collected in the visible and thermal parts of the electromagnetic spectrum and can reduce spatial coverage such that an assessment of the near-IR and thermal conditions of the ice shelf surface cannot be determined on a daily basis. Therefore, 8-day composited data will be used in this analysis. While this retrieval scheme will have lower temporal resolution than standard passive microwave techniques, our method will allow for the determination of melt water fraction in the firn whereas active and passive microwave methodologies only detect the presence or absence of melt above some fixed threshold. Our retrieval method is executed over the Ross Ice Shelf, because it has a high density of surface meteorology stations necessary to calibrate the emperical liquid water fraction retrieval model.

The calibration phase of this effort involves using SNTHERM89 to produce estimates of snow pack near surface bulk liquid water content. SNTHERM89 is a one-

TCD
3, 1069–1107, 2009

dimensional mass and energy balance model for estimating mass and energy flux through strata of snow and soil. It is comprehensive in scope, capable of simulating dynamic processes (Jordan, 1991). The version used in this project was adapted to estimate model snow melt conditions over glacier ice, which involved adding ice material properties to the SNTHERM89 material library (modifications courtesy of S. Frankenstein, CRREL).

SNTHERM89 was forced (Fig. 2, boxes 1, 2, 3) using 2m air temperature (AWS), relative humidity (AWS), wind speed (AWS), downwelling shortwave (NSF UV/Vis), reflected shortwave (NSF UV/Vis multiplied by albedo calculated from NCEP/NCAR reanalysis), downwelling longwave (NCEP/NCAR Reanalysis) and precipitation amount (NCEP/NCAR Reanalysis). In addition to the meteorological forcing data, SNTHERM89 also requires precipitation type and effective diameter of precipitation as input. It was assumed for the purposes of this study that precipitation remained frozen, with an effective diameter of 0.5 mm. SNTHERM89 initialization snowpack stratigraphy was supplied by K. Steffen (personal communication, 2001) from a snow pit dug on the Greenland ice sheet. While not necessarily representative of initial conditions on the Ross Ice Shelf, sensitivity tests performed show that SNTHERM89 responds quickly to atmospheric forcing such that melt conditions in the upper layers are not dependant on the initial conditions after about 72 h.

SNTHERM89 was run at 6-hourly time steps over the two month study period (Fig. 2, box 4). LWF in the upper 1 cm of the snowpack (Fig. 2, box 5) were used as representative of the skin through which the MODIS satellite can collect reflectance and thermal information. Daily LWF was recorded at 12 z, which is closest to the MODIS overpass time, and averaged over each 8-day composite period for each site. The calibration phase is the creation of a 3-dimensional planar regression between LWF (dependant variable) and MODIS band 5 reflectance and MODIS-derived skin temperature (independent variables, Fig. 2, box 6) for each composite period and each study site (Fig. 2, box 7). From this regression, a relationship for LWF as a function of reflectance and thermal signature was developed (Fig. 2, box 8). This function was applied to the entire

Ross Ice Shelf (Fig. 2, box 9) where MODIS band 5 reflectance and MODIS skin temperature are known, but melt fraction is unknown – the empirical retrieval of effective melt fraction, $LWF_{<eff>}$ (Fig. 2, box 10).

Table 1 is a comparison of the spatial, temporal, and melt resolutions of three methods for assessing surface melt. XPGR has a coarser spatial resolution than the coupled near-IR/thermal method, and neither QuikSCAT nor XPGR are able to resolve effective liquid water fraction to obtain a magnitude of surface melt. The coupled near-IR/thermal method is limited in that the temporal resolution is 8-day rather than the daily resolution offered by XPGR or QuikSCAT.

6 Results

6.1 Melt magnitude retrieval model results

The coupled near-IR/thermal retrieval model shows little to no melt for five of the seven composite periods and spatially-constrained areas of low liquid water fraction (0.5–1%) for the other two composite periods. Throughout most of December, most of the Ross Ice Shelf experiences no surface melting at all. An increase in surface melt fractions is seen during the 2–9 January composite period over the western half of the ice shelf (Fig. 3). This is followed by a refreeze during the 10-17 January period (Fig. 4), and a spatially expansive surface melt event on the eastern portion of the ice shelf from 18–25 January (Fig. 5). While the two detected melt events (2–9 January and 18–25 January) were spatially coherent, the magnitude of the surface melting was low (1% or less) in both cases.

During the 2–9 January melt event there is both a signature in reflection and IST that is consistent with a low $LWF_{<eff>}$ melting event. Temperatures in the >0.5% melt are are slightly above 269 K. A transect of $LWF_{<eff>}$, reflectance and surface temperature through the area experiencing melt (Fig. 6) shows that there is a strong signal in the reflectance associated with higher $LWF_{<eff>}$ values, and ambient temperatures that

TCD
3, 1069–1107, 2009

are marginal, but close enough to freezing that some melt may be occurring. While temperatures remain ~4 K below freezing, it is possible that surface melt is occurring if there is some temperature heterogeneity over the 8-day composite period and over the spatial extent of the 4 km grid size. This melt event was marginal, and with a spatial distribution that would be difficult to detect in passive microwave analyses.

6.2 XPGR comparison

The coupled near-IR/thermal melt magnitude retrieval model shows generally good agreement with passive microwave XPGR melt occurrence. Of the seven composite periods in the December–January study period, five exhibited little to no surface melting anywhere on the ice shelf, one showed melt in a coincident time and place between the two melt assessments (18–25 January), and one had some discrepancies between the two melt retrieval methods (2–9 January) where XPGR showed no melting and the coupled near-IR/thermal method showed discontinuous areas on the western half of the ice shelf of 0.5 to 1% $LWF_{<eff>}$.

The largest spatially contiguous area of surface melting is found during the last (18–25 January) composite period (Fig. 5), where large areas of the Ross Ice Shelf surrounding Roosevelt Island show as much as 1% surface melting. This melting is seen in both the XPGR surface melt analysis as well as the near-IR/thermal effective melt retrieval, and both methods show the melt as being both spatially and temporally consistant with one another. Effective melt magnitudes range from 0.5% to 1% during this time period within the areas shown by XPGR to be experiencing surface melting. XPGR detected surface melting during one to five of the eight days of the composite period, so it is likely that surface melt magnitudes were in excess of 1% for part of the composite period, even though the average melt over the entire 8-day composite period was below the 1% threshold for XPGR detection.

We further evaluate our MODIS derived melt magnitude by examining how $LWF_{<eff>}$ varies with melt duration (the number days melt was detected) at any given location on the ice sheet. We accomplished this by calculating a mean $LWF_{<eff>}$ of all pixels

that correspond to particular melt duration (number of melt days) as determined from XPGR within each 8-day composite period (Fig. 7). A comparison between $LWF_{<eff>}$ and XPGR melt duration for the 18–25 January composite period shows the lowest $LWF_{<eff>}$ values (average of 0.29%) correspond to XPGR melt duration of zero days. Slightly higher $LWF_{<eff>}$ (average of 0.43%) are seen for an XPGR melt duration of one day. At XPGR melt durations of two to five days, average $LWF_{<eff>}$ was between 0.53% and 0.54%, indicating only slightly higher $LWF_{<eff>}$ values for XPGR melt durations of 5 days than for XPGR melt durations of 2 days. During this melt event, XPGR did not detect any areas with melt durations of longer than five days.

7 Model validation and uncertainty

Model verification was accomplished using the Cross-Polarized Gradient Ration (XPGR, Abdalati and Steffen, 1995; Abdalati and Steffen, 1997) over the Ross Ice Shelf for coincident time periods. This method provides a binary indication of melt occurrence, and is sensitive to changes in the dielectric constant of ice as surface liquid water fractions rise above 1%. While daily XPGR were calculated, these were aggregated to the same 8-day composite scales found in the MODIS archive for a more direct comparison of the two melt characterization methods. Therefore, the number of melt days for each pixel during each MODIS 8-day composite period is presented.

Several sensitivity tests were performed to analyze the effects of downscaling uncertainty from the use of gridded NCEP/NCAR reanalysis output as SNTHERM input variables. While NCEP/NCAR incoming shortwave radiation output was not used in the calibration of LWF in this study, variation in radiation input can nevertheless be insightful as to the degree to which uncertainty in radiation input to SNTHERM can affect liquid water fraction. Precipitation and radiation measurements were estimated from reanalysis output for each of the locations, and to test how SNTHERM responded to changes in these variables, several melt simulations were calculated for Pegasus South using 2×, 4× and 0.5× precipitation (Fig. 8), and incoming shortwave radiation

plus 5% and minus 5% (Fig. 9). The changes in incoming solar radiation represent potential levels of downscaling uncertainty in cloud cover over the reanalysis grid cell. From these runs, it was clear that precipitation has little effect, less than 1% LWF, on the melt characterization at Pegasus South. While precipitation rates can vary within the area comprising a reanalysis grid cell, these variations would not induce large changes in surface LWF within the cell. Larger changes were seen in the radiation sensitivity test. Increasing the downward flux of shortwave radiation by 5% doubled the liquid water fraction at the test site, whereas decreasing the radiation flux by 5% halved the liquid water fraction. Uncertainty in the downscaling of radiation flux can have a significant effect on SNTHERM output, which can therefore cause uncertainty in the E-melt empirical retrieval model. If accurate radiation measurements were obtainable at each of the AWS sites, a more precise estimation of surface $LWF_{<eff>}$ could be obtained using the coupled near-IR/thermal method.

Another sensitivity test was used to determine the effects of the SNTHERM initialization stratigraphy on surface LWF (Fig. 10). Observed temperatures at depth for December, 2007 at Nascent Iceberg, Ross Ice Shelf, supplied by Doug MacAyeal were substituted into the original SNTHERM stratigraphy. This caused a net change in surface LWF of less than 1% for each of the December composite periods. Little variation was seen even in the LWF values at the daily scale. As the SNTHERM model responds quickly to meteorological forcing conditions, it can be assumed that differences in the initialization parameters have little effect on surface melt output. Consequently, as long as a reasonable initialization stratigraphy is used, there should be little influences on surface LWF values from subtle differences in firn stratigraphy.

As this emperical model contains many data sources, there are several potential error sources that need to be accounted for (Table 2). The relative error contribution from MODIS data includes 0.38% from IST (Wan et al., 2002; Hall et al., 2004) and 2% from reflectance (Liang et al., 2002). Resistances in AWS thermistors are known to within 1% and anemometors are calibrated to a 0.5% tolerance (Stearns et al., 1993). Sensitivity analyses show that a doubling of precipitation creates a 0.5% variation,

and varying radiation by ±5% can affect LWF values by 1.4%. The standard error of regression for the planar retrieval model was 0.5%. The total relative error in this study was 2.8%.

8 Discussion

In general, the two methodologies for assessing surface melt conditions, XPGR and the coupled near-IR/thermal method for calculating effective melt magnitude are consistent with one another. Effective melt magnitudes were low, mostly 0–0.5% where XPGR did not detect any surface melting, and slightly higher, mostly 0.5–1%, where XPGR detected melting. While this would correspond to only the most marginal of melt events for an area such as the Antarctic Peninsula, it was a fairly substantial surface melting event for the much colder Ross Ice Shelf. The coupled near-IR/thermal method is particularly useful for detecting fine-scale melt events that are unresolvable by passive microwave techniques, as well as the magnitude of large melt events, which is not currently possible to retrieve through other means.

One melt event that was not detected through XPGR or other passive microwave methodologies was identified in the 2–9 January composite period. Melt signatures associated with strong downsloping winds are especially evident in the center of the ice shelf at this time. Strong southerly winds were identified by NCEP/NCAR reanalysis (Fig. 11) over the eastern half of the Ross Ice Shelf. Effective melt is shown to increase at this time over the center of the ice shelf spatially coincident with the path of these katabatic-like winds. This increase in effective melt is not identified by XPGR and could be explained as either a coarsening of grains as a result of wind sorting, or an increase in surface melt fraction that is not yet high enough (or at a spatial scale large enough) to cause changes in the bulk dielectric constant of the surface at the 25 km resolution, and therefore cannot be detected through passive microwave imagery. Bromwich (1989) noted that katabatic wind strength can be identified in warm thermal IR signatures, which understandably are manifested in the surface melt magnitude which is derived

TCD
3, 1069–1107, 2009

using the thermal IR band.

By the middle of January (Fig. 4), large areas of the ice sheet begin to show little effective melt again, and the katabatic-like regime of the previous composite period begins to weaken. Analysis during this period is complicated by the persistent cloud cover over most of the eastern half of the ice sheet, and large portions of the western half as well, though cloud-free pixels in this region clearly show what appears to be a re-freeze taking place. Southwesterly winds predominate over the ice sheet during this period, inhibiting any influence of the offshore polynyas.

The 18–25 January composite period was the more substantial melt event and was detected by both XPGR and the coupled near-IR/thermal methods. The surface melting during this period corresponded to weak, onshore surface winds on the eastern half of the ice shelf, as shown in the reanalysis images (Fig. 12) in the areas where the melt was occurring. This suggests that the maritime influence of surface air blowing over a near-shore polynya may contribute to conditions that are conducive to surface melting. Near McMurdo, which was not identified as an area experiencing surface melt in XPGR, stronger offshore winds seemed to inhibit the generation of surface melt.

The comparison between average $LWF_{<eff>}$ at 25 km^2 resolution and XPGR (Fig. 7) showed monotonic increase in $LWF_{<eff>}$ for XPGR melt duration of zero, one, and two days, with a saturation in $LWF_{<eff>}$ at an XPGR melt duration of 2 days or longer. This saturation effect is likely the result of low amounts of surface melting during this event, with no areas receiving greater than 1% surface liquid water fraction during any composite period. The sample size for the XPGR melt durations of four and five days were each less than ten pixels, while the number of pixels with zero day melt duration was greater than 400. For XPGR, there is evidence from this comparison that the category of no-melt, or zero days of occurrence consistently exhibits effective melt fractions between 0–0.4% and can be slightly higher (0.3–0.5%) for a single occurrence throughout the composite period. Abdalati and Steffen (1997) specify that the XPGR threshold will register a pixel as melting when surface liquid water fractions by volume are in excess of 1%. While no pixels showed $LWF_{<eff>}$ values of greater than 1%, no

TCD
3, 1069–1107, 2009

pixels experienced melt every day during the compisite period. A refreezing during part of the composite period would effectively dilute a marginal melt event such that the $LWF_{<eff>}$ would be beneath 1% when aggregated over 8-days.

While the coupled near-IR/thermal methodology for effective melt fraction retrieval shows promise, further calibration is necessary for useful effective melt retrieval over warm ice shelves such as Larsen. Current calibration is only useful for detection of surface melt magnitude of 2.5% or less. In addition, the feature space created during the calibration process is not necessarily best represented by a planar correlation. Surface melting cannot occur with surface temperatures below freezing, but because of variations in surface temperature within a spatially heterogenous pixel, a fixed 273 K cutoff for surface melting is not realistic. There likely is some temperature below which melt water cannot be present, even if grains are particularly coarse. To remedy this problem, an investigation using artificial neural networking to generate a calibration curve is currently in progress. Such a calibration procedure would allow for non-linear response of liquid water fraction to changes in surface temperature and reflectance.

9 Conclusions

The coupled near-IR/thermal method for assessing surface melt offers several benefits over passive microwave and microwave scatterometry (Table 1). The spatial resolution is higher than passive microwave and the coupled near-IR/thermal method can therefore detect melt events that are occurring on a smaller spatial scale. The ability to retrieve surface melt magnitude is another improvement over both passive microwave and microwave scatterometry. The most significant drawback of the coupled near-IR/thermal methodology is the decrease in temporal resolution from daily to 8-day. The coupled near-IR/thermal methodology, while providing important information regarding the state of surface melt on Antarctic ice shelves, is not meant to replace traditional methods for detecting surface melt presence, such as XPGR. Rather, when used in concert with these methods, the coupled near-IR/thermal method can provide a quan-

titative estimate of melt fraction which has not previously been available through other remote sensing methodologies.

Acknowledgements. The authors would like to thank Doug MacAyeal and Konrad Steffen for supplying information used to construct the initialization stratigraphy for SNTHERM. Many thanks also to Steve Daly and Sally Shoop from CRREL for providing information regarding the NSF radiation data for McMurdo station. We would also like to thank Richard Alley, Sridhar Anandakrishnan, and the rest of the PSICE research group at Penn State University for their insight and feedback on this project. Thanks also to Andrew Carleton and Michael Mann for additional feedback. Thanks also to Terry Haran from NSIDC for providing the MODIS Ice Surface Temperature dataset used in this analysis. NCEP Reanalysis data provided by the NOAA/OAR/ESRL PSD, Boulder, Colorado, USA, from their Web site at http://www.cdc.noaa.gov. This work was funded through NASA Grant Number: NNX06AE50G.

References

Abdalati, W. and Steffen, K.: Passive Microwave-Derived Snow Melt Regions on the Greenland Ice Sheet, Geophys. Res. Lett., 22, 787–790, 1995.

Abdalati, W. and Steffen, K.: Snowmelt on the Greenland Ice Sheet as Derived from Passive Microwave Satellite Data, J. Climate, 10, 165–175, 1997.

Bohren, C.: Applicability of effective-medium theories to problems of scattering and absorption by nonhomogeneous atmospheric particles, J. Atmos. Sci., 43, 468–475, 1986.

Bohren, C. and Barkstrom, B.: Theory of the optical properties of snow, J. Geophys. Res., 79, 4527–4535, 1974.

Bromwich, D. H.: Satellite Analyses of Antarctic Katabatic Wind Behavior, B. Am. Meteorol. Soc., 70, 738–749, 1989.

Bromwich, D. H. and Fogt, R. L.: Strong Trends in the Skill of the ERA-40 and NCEP-NCAR Reanalyses in the High and Midlatitudes of the Southern Hemisphere, 1958–2001, J. Climate, 17, 4603–4619, 2004.

Cavalieri, D., Markus, T., and Comiso, J.: AMSR-E/Aqua Daily L3 12.5 km Brightness Temperature, Sea Ice Concentration, & Snow Depth Polar Grids V002, 1 December 2002–31 January 2003, Boulder, Colorado USA: National Snow and Ice Data Center, Digital media, updated daily, 2004.

Colbeck, S. C.: An Overview of Seasonal Snow Metamorphism, Reviews of Geophysics and Space Physics, 20, 45–61, 1982.
Colbeck, S.: Snow-crystal Growth with varying surface temperatures and radiation penetration, J.Glaciol., 35, 23–29, 1989.
Doake, C. S. M. and Vaughan, D. G.: Rapid Disintegration of the Wordie Ice Shelf in Response to Atmospheric Warming, Nature, 350, 328–330, 1991.
Dozier, J.: Spectral Signature of Alpine Snow Cover from the Landsat Thematic Mapper, Remote Sens. Environ., 28, 9–22, 1989.
Fettweis, X., van Ypersele, J.-P., Gallée, H., Lefebre, F., and Lefebvre, W.: The 1979–2005 Greenland ice sheet melt extent from passive microwave data using an improved version of the melt retrieval XPGR algorithm. Geophys. Res. Lett., 34, L05502, doi:10.1029/2006GL028787, 2007.
Grenfell, T., Perovich, D., and Ogren, J.: Spectral albedo of an alpine snowpack, Cold Reg. Sci. Tech., 4, 121–127, 1981.
Hall, D. K., Riggs, G. A., and Salomonson, V. V.: MODIS/Aqua Sea Ice Extent and IST Daily L3 Global 4 km EASE-Grid Day V005, 1 December 2002–25 January 2003, Boulder, Colorado USA: National Snow and Ice Data Center, Digital media, updated daily, 2007.
Hyvärinen, T. and Lammasniemi, J.: Infrared Measurement of Free-Water Content and Grain Size of Snow, Opt. Eng., 26, 342–348, 1987.
Jezek, K., Gogineni, P., and Shanableh, M.: Radar Measurements of Melt Zones on the Greenland Ice Sheet, Geophys. Res. Lett., 21, 33–36, 1994.
Jordan, R.: A One-Dimensional Temperature Model for a Snow Cover, Technical Documentation for SNTHERM89, 1991.
Kalnay, E., Kanamitsu, M., Kistler, R., Collins, W., Deaven, D., Gandin, L., Iredell, M., Saha, S., White, G., Woollen, J., Zhu, Y., Leetmaa, A., and Reynolds, B.: The NCEP/NCAR Reanalysis 40-year Project, B. Am. Meteorol. Soc., 77, 437–471, 1996.
King, J. C., Turner, J., Marshall, G. J., Connolley, W. M., and Lachlan-Cope, T. A.: Antarctic Peninsula Climate Variability and its Causes as Revealed by Analysis of Instrumental Records. British Antarctic Survey, Natural Environment Research Council, 2002.
Lampkin, D. and Peng, R.: Empirical Retrieval of Surface Melt Magnitude from Coupled MODIS Optical and Thermal Measurements over the Greenland Ice Sheet during the 2001 Ablation Season, Sensors, 8, 4915–4947, 2008.
Lampkin, D. J. and Yool, S. R.: Monitoring Mountain Snowpack Evolution Using Near-Surface

Optical and Thermal Properties, Hydrol. Process., 18, 3527–3542, 2004.
Liang, S., Fang, H., Chen, M., Shuey, C. J., Walthall, C., Daughtry, C., Morisette, J., Schaaf, C., and Strahler, A.: Validating MODIS land surface reflectance and albedo products: methods and preliminary results, Remote Sens. Environ., 83, 149–162, 2002.
MacAyeal, D. R.: Irregular Oscillations of the West Antarctic Ice Sheet, Nature, 359, 29–32, 1992.
Marks, D. and Dozier, J.: Climate and energy exchange at the snow surface in the alpine region of the Sierra Nevada, 2: Snow cover energy balance, Water Resour. Res., 28, 3043–3054, 1992.
Mätzler, C., Aebischer, H., and Schanda, E.: Microwave dielectric properties of surface snow. (Invited) IEEE J. Ocean. Eng., OE-9, 366–371, 1984.
Mätzler, C. and Hüppi, R.: Review of Signature Studies for Microwave Remote Sensing of Snowpacks, Adv. Space Res., 9(1), 253–265, 1989.
Mote, T. L.: Greenland surface melt trends 1973-2007: Evidence of a large increase in 2007, Geophys. Res. Lett., 34, L22507, doi:10.1029/2007GL031976, 2007.
Mote, T. and Anderson, M.: Variations in snowpack melt on the Greenland ice sheet based on passive microwave-measurements, J. Glaciol., 41, 51–60, 1995.
Nghiem, S. V., Steffen, K., Kwok, R., and Tsai, W.-Y.: Detection of Snowmelt Regions on the Greenland Ice Sheet using Diurnal Backscatter Change, J. Glaciol., 47, 539–547, 2001.
Nolin, A. W. and Dozier, J.: A Hyperspectral Method for Remotely Sensing the Grain Size of Snow, Remote Sens. Environ., 74, 207–216, 2000.
Painter, T., Dozier, J., Roberts, D., Davis, R., and Green, R.: Retrieval of subpixel snow-covered area and grain size from imaging spectrometer data, Remote Sens. Environ., 85, 64–77, 2003.
Peng, R.: Estimation of surface melt intensity using optical and thermal measurements over the Greenland ice sheet, M. S. thesis, Department of Geography, Pennsylvania State University, 2007.
Ridley, J.: Surface Melting on Antarctic Peninsula Ice Shelves Detected by Passive Microwave Sensors. Geophys. Res. Lett., 20, 2639–2642, 1993.
Scambos, T. A., Bohlander, J. A., Shuman, C. A., and Skvarca, P.: Glacier Acceleration and Thinning after Ice Shelf Collapse in the Larsen B Embayment, Antarctica, Geophys. Res. Lett., 31, L18402, doi:10.1029/2004GL020670, 2004.
Scambos, T. A., Hulbe, C., Fahnestock, M., and Bohlander, J.: The link between climate warm-

ing and break-up of ice shelves in the Antarctic Peninsula, J. Glaciol., 46, 516–530, 2000.
Sergienko, O. and MacAyeal, D. R.: Surface Melting on the Larsen Ice Shelf, Antarctica, Ann. Glaciol., 40, 215–218, 2005.
Smith, S. D., Muench, R. D., and Pease, C. H.: Polynyas and Leads: An Overview of Physical Processes and Environment, J. Geophys. Res., 95, 9461–9479, 1990.
Steffen, K., Nghiem, S. V., Huff, R., and Neumann, G.: The Melt Anomaly of 2002 on the Greenland Ice Sheet from Active and Passive Microwave Satellite Observations. Geophys. Res. Lett., 31, L20402, doi:10.1029/2004GL020444, 2004.
Steig, E. J., Schneider, D. P., Rutherford, S. D., Mann, M. E., Comiso, J. C., and Shindell, D. T.: Warming of the Antarctic Ice Sheet Surface since the 1957 International Geophysical Year, Nature, 457, 459–462, 2009.
Stearns, C. R., Keller, L. M., Weidner, G. A., and Stevens, M.: Monthly Mean Climatic Data for Antarctic Automatic Weather Stations, in: Antarctic Meteorology and Climatology: Studies Based on Automatic Weather Stations, AGU Antarctic Research Series, American Geophysical Union, Washington, DC, 1–21, 1993.
Stearns, C.: Automatic Weather Station Project, University of Wisconsin-Madison, funded by the National Science Foundation of the United States of America, ongoing, 2009.
Tedesco, M.: Snowmelt Detection over the Greenland Ice Sheet from SSM/I Brightness Temperature Daily Variations, Geophys. Res. Lett., 34, L02504, doi:10.1029/2006GL028466, 2007.
Tiuri, M. E., Sihvola, A. H., Nyfors, E. G., and Hallikaiken, M. T.: The Complex Dielectric Constant of Snow at Microwave Frequencies. (Invited) IEEE J. Ocean. Eng., OE-9, 377–382, 1984.
Turner, J., Colwell, S. R., Marshall, G. J., Lachlan-Cope, T. A., Carleton, A. M., Jones, P. D., Lagun, V., Reid, P. A., and Iagovkina, S.: Antarctic Climate Change during the Last 50 Years, Int. J. Climatol., 25, 279–294, 2005.
van den Broeke, M.: Strong Surface Melting Preceded the Collapse of Antarctic Peninsula Ice Shelf, Geophys. Res. Lett., 32, L12815, doi:10.1029/2005GL023247, 2005.
Wan, Z., Zhang, Y., Zhang, Q., and Li, Z.-L.: Quality assessment and validation of the MODIS global land surface temperature, Int. J. Remote Sens., 25(1), 261–274, 2004.
Warren, S. G.: Optical Properties of Snow, Reviews of Geophysics and Space Physics, 20, 67–89, 1982.
Warren, S. G. and Wiscombe, W. J.: A Model for the Spectral Albedo of Snow. II: Snow Con-

taining Atmospheric Aerosols, J. Atmos. Sci., 37, 2734–2745, 1980.
Wiscombe, W. J. and Warren, S. G.: A Model for the Spectral Albedo of Snow. I: Pure Snow, J. Atmos. Sci., 37, 2712–2733, 1981.
Zwally, H. J.: Microwave Emissivity and Accumulation rate of Polar firn, J. Glaciol., 18(79), 195–215, 1977.
Zwally, H. J., Comiso, J. C., and Gordon, A. L.: Antarctic Offshore Leads and Polynyas and Oceanographic Effects, in: Oceanology of the Antarctic Continental Shelf, Antarctic Research Series, edited by: Jacobs, S. S., AGU, Washington, DC, 203–226, 1985.
Zwally, H. and Fiegles, S.: Extent and duration of Antarctic surface melt, J. Glaciol., 40, 463–476, 1994.

Table 1. Comparison of various methods for assessing surface melt

	XPGR (Passive Microwave)	QuikSCAT Backscatter (Microwave Scatterometer)	Coupled near-IR/Thermal IR
Spatial Resolution	12.5–25 km	2.225 km	1–4 km
Temporal Resolution	Daily	Daily	8-day
Melt Resolution	Binary	Binary	Magnitude

TCD
3, 1069–1107, 2009

Table 2. Relative error estimates.

Error Source	Error Amount	Citation
Ice Surface Temperature	±0.38% (1˚C)	Wan et al., 2002; Hall et al., 2004
Reflectance	±2%	Liang et al., 2002
Precipitation	±0.5%	Sensitivity Testing
Radiation	±1.4%	Sensitivity Testing
AWS Thermistor Error	±1%	Stearns et al., 1993
AWS Anemometor Error	±0.5%	Stearns et al., 1993
Regression Error	±0.5%	Standard Error
Total Relative Error	±2.8%	

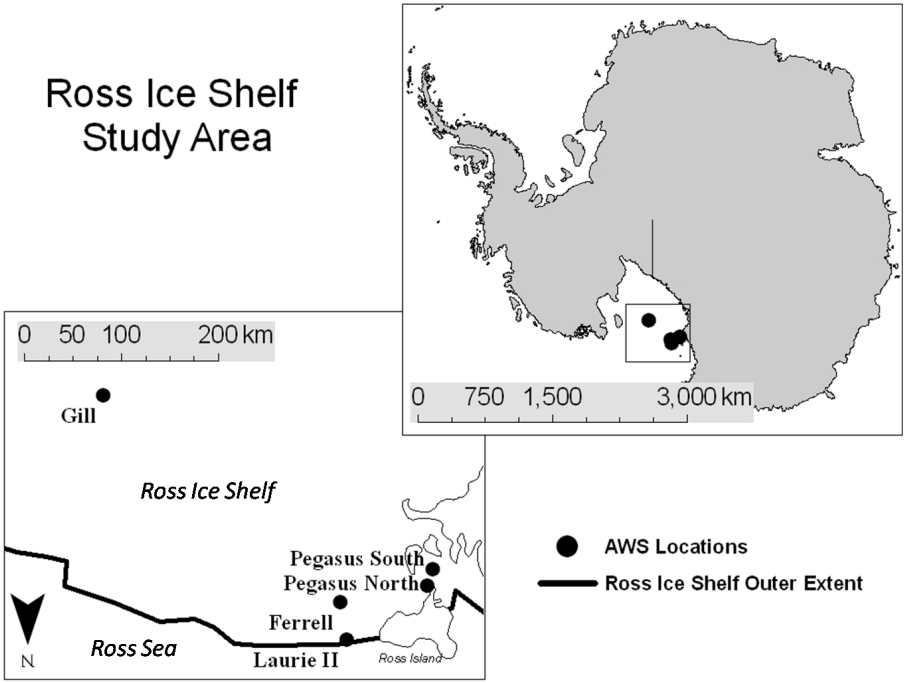

Fig. 1. Ross Ice Shelf Study area with AWS reference stations.

TCD
3, 1069–1107, 2009

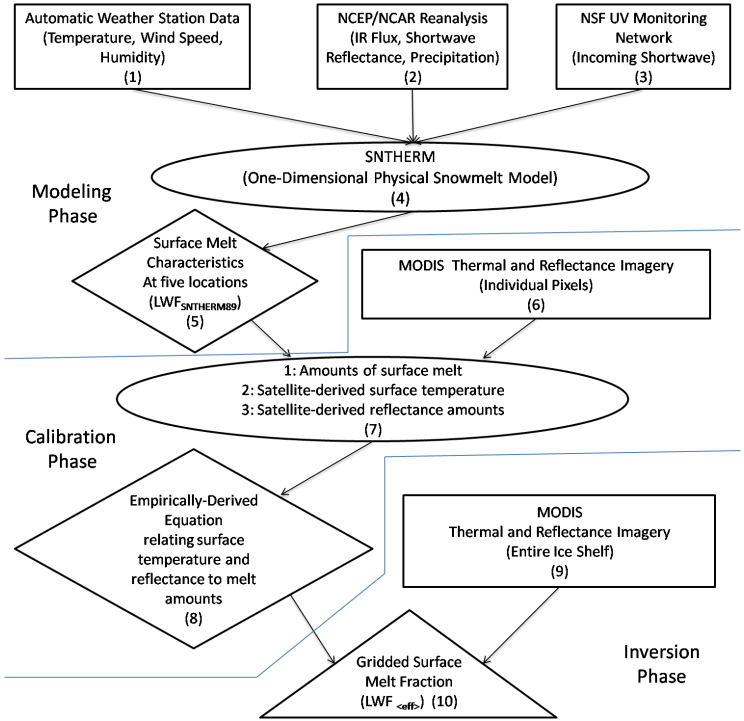

Fig. 2. Process flowchart for retrieval of surface effective liquid water fraction ($LWF_{<eff>}$) derived from coupled MODIS Near-IR/Thermal signatures. (Rectangle=Primary Data Source, Oval=Processes, Diamond=Intermediate Output, Triangle=Primary output).

TCD
3, 1069–1107, 2009

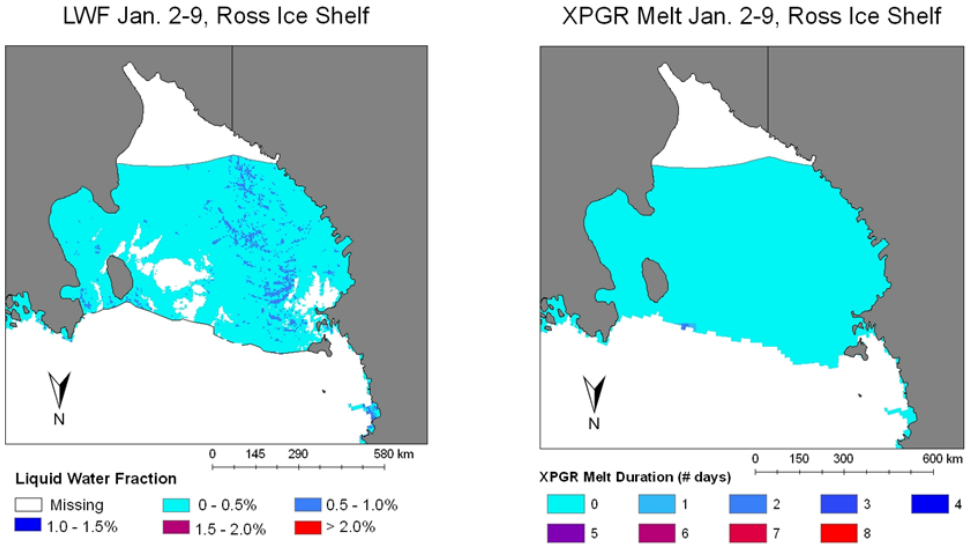

Fig. 3. Effective Surface Melt Magnitude (left) and XPGR melt occurrence (right) for Composite Period 2–9 January, 2003. Missing Data includes data that is unusable due to cloud cover.

TCD
3, 1069–1107, 2009

D. J. Lampkin and C. C. Karmosky

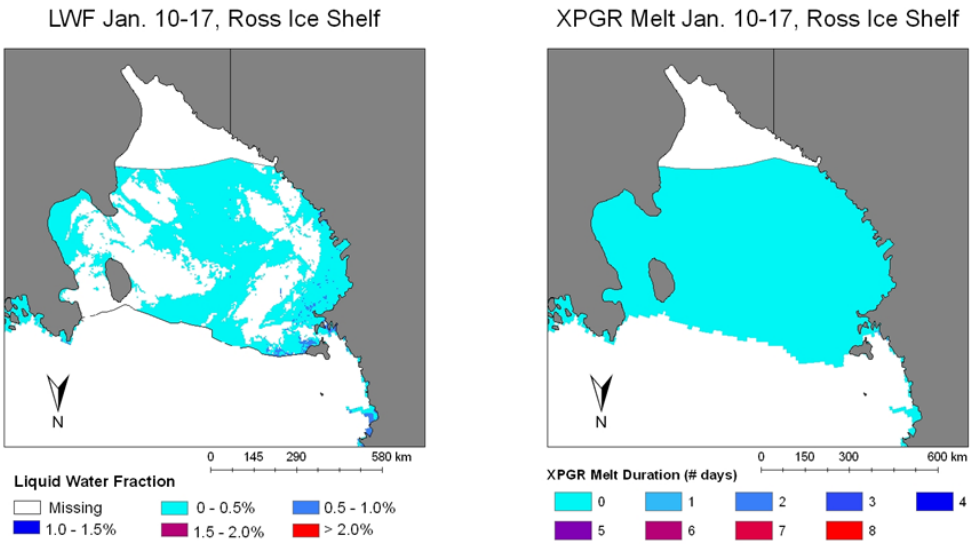

Fig. 4. Effective Surface Melt Magnitude (left) and XPGR melt occurrence (right) for Composite Period 10–17 January, 2003. Missing Data includes data that is unusable due to cloud cover.

TCD
3, 1069–1107, 2009

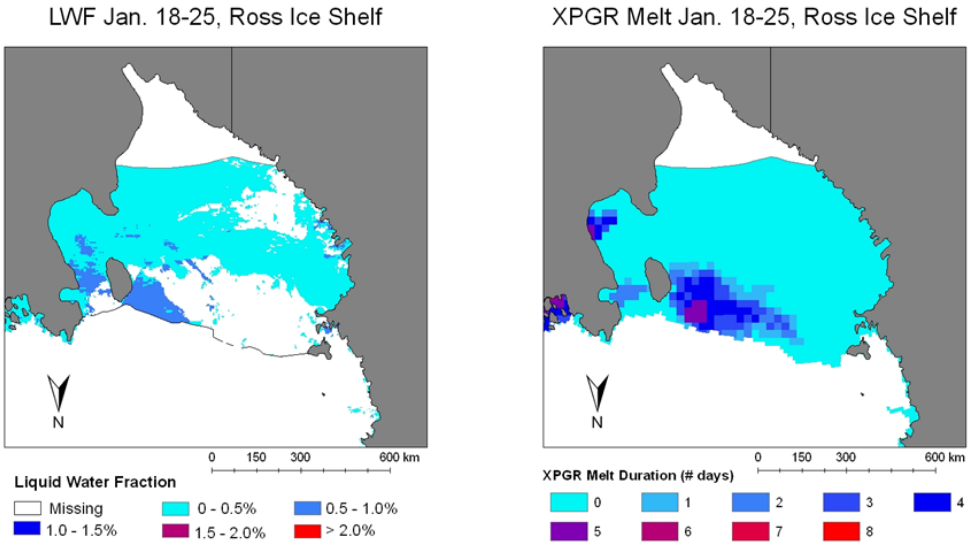

Fig. 5. Effective Surface Melt Magnitude (left) and XPGR melt occurrence (right) for Composite Period 18–25 January, 2003. Missing Data includes data that is unusable due to cloud cover.

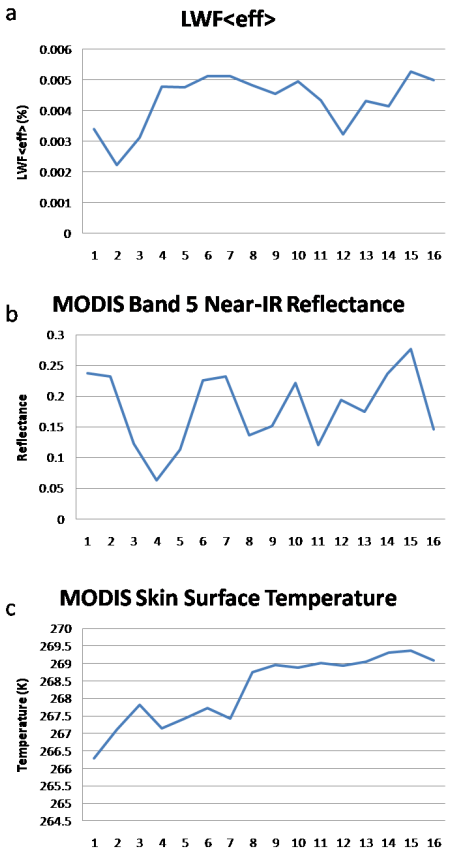

Fig. 6. E–W Transect through low $LWF_{<eff>}$ melt area on Ross Ice Shelf, **(a)** Surface Effective Liquid Water Fraction ($LWF_{<eff>}$), **(b)** MODIS band 5 surface reflectance, **(c)** MODIS-derived surface skin temperature.

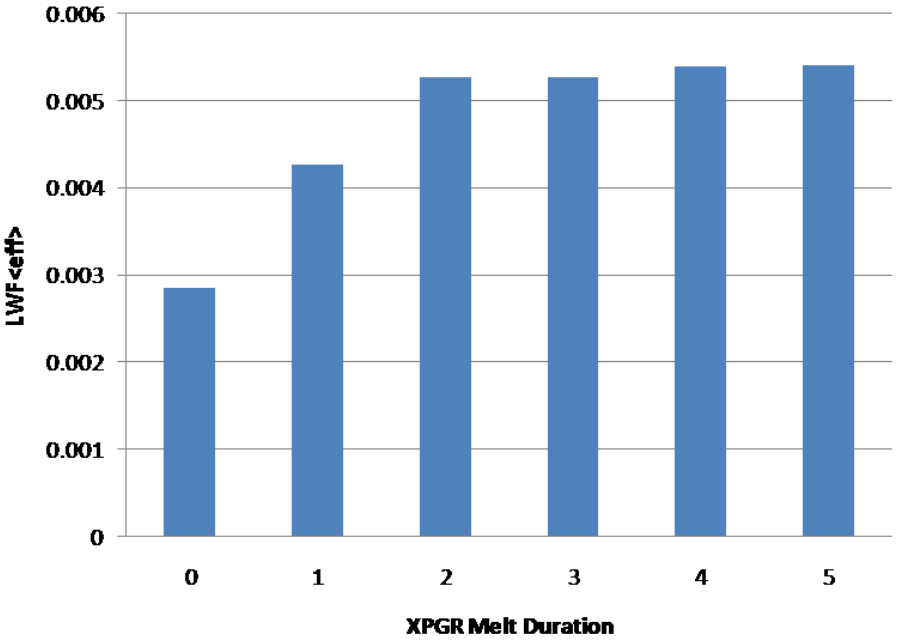

Fig. 7. Histogram comparison of $LWF_{<eff>}$ to XPGR Melt Duration. Bars represent average $LWF_{<eff>}$ for all pixels corresponding to a particular melt duration as determined by XPGR.

TCD
3, 1069–1107, 2009

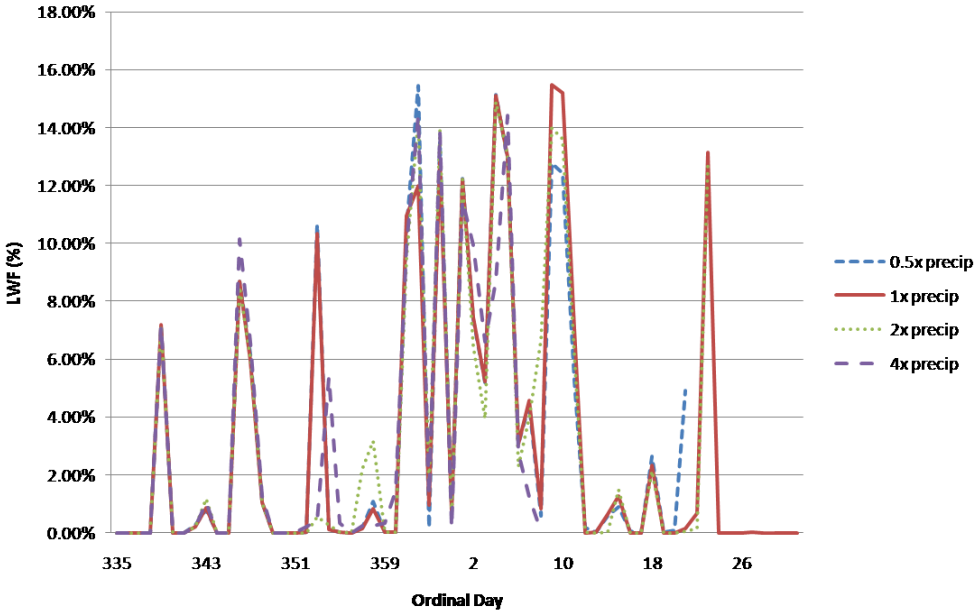

Fig. 8. Precipitation Sensitivity Analysis at 8-day composite (top) and Daily (bottom) time intervals using NCEP/NCAR Reanalysis Radiation data and 0.5× NCEP/NCAR precipitation, 1× NCEP/NCAR precipitation, 2× NCEP/NCAR precipitation and 4× NCEP/NCAR precipiation for SNTHERM forcing at Pegasus South station.

TCD
3, 1069–1107, 2009

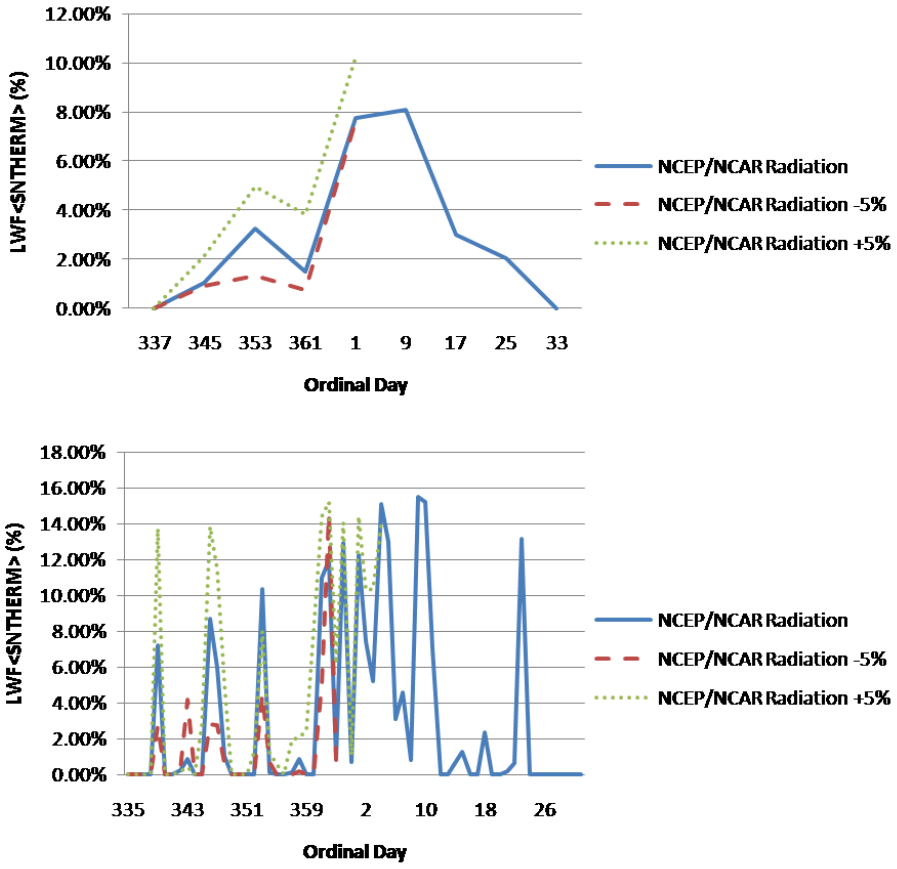

Fig. 9. Radiation Sensitivity Analysis at 8-day composite (top) and Daily (bottom) time intervals using variations in NCEP/NCAR radiation data as forcing for SNTHERM at Pegasus South Station.

TCD
3, 1069–1107, 2009

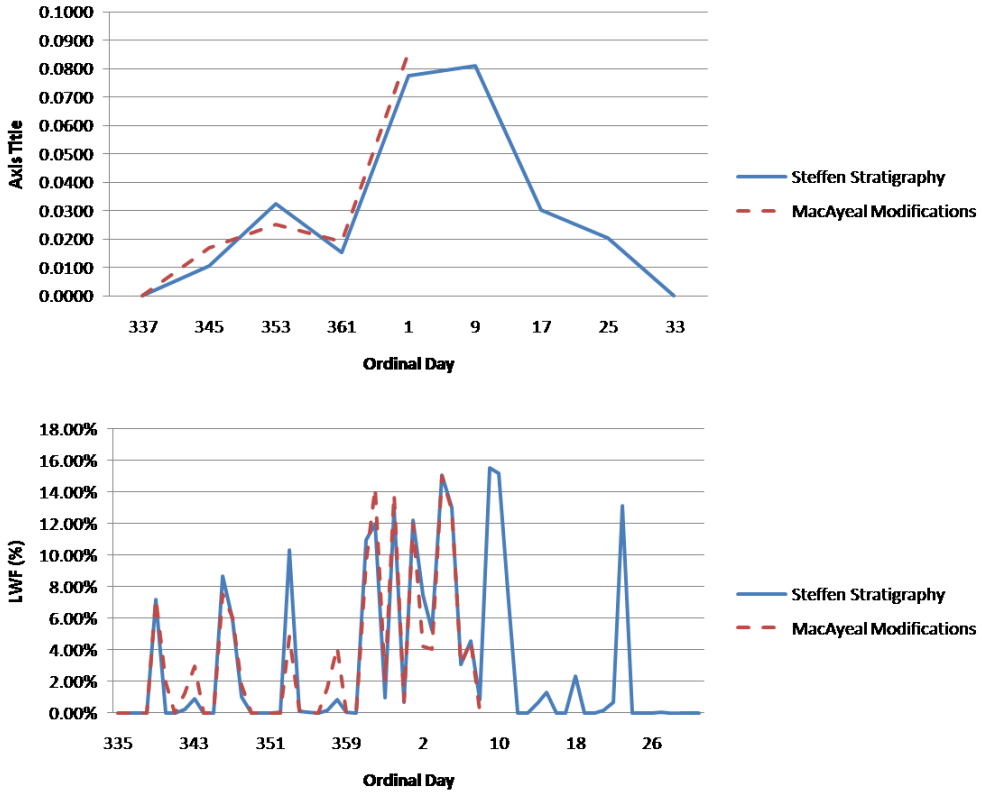

Fig. 10. Stratigraphy Sensitivity Analysis at 8-day composite (top) and Daily (bottom) time intervals using NCEP/NCAR radiation forcing for SNTHERM at Pegasus South Station.

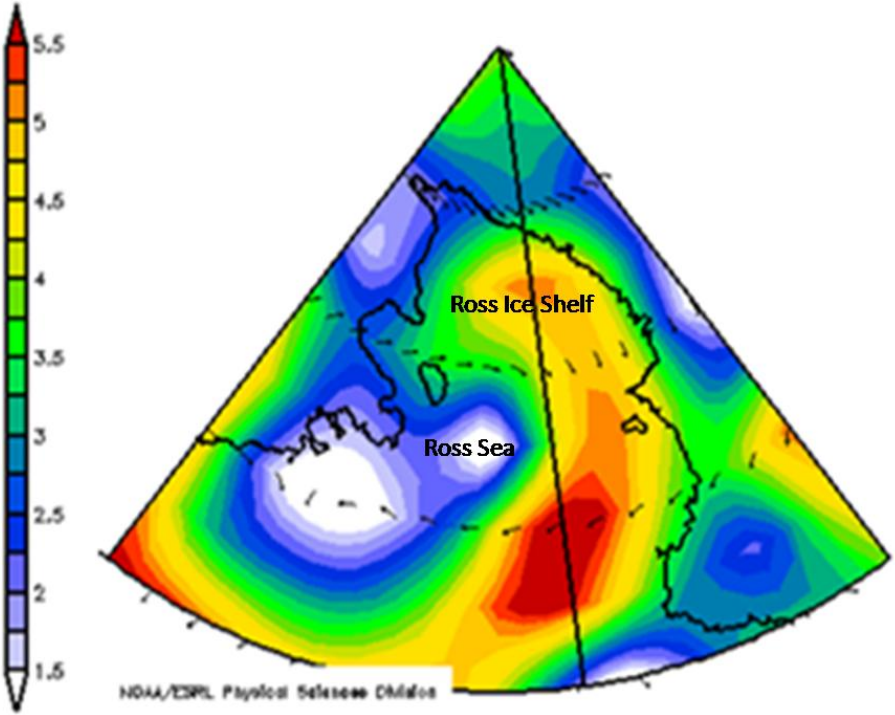

Fig. 11. Reanalysis-Derived Surface Vector Wind Speed (m/s) and Direction for 2–9 January composite period. Image provided by the NOAA/ESRL Physical Sciences Division, Boulder Colorado from their Web site at http://www.esrl.noaa.gov/psd/.

TCD
3, 1069–1107, 2009

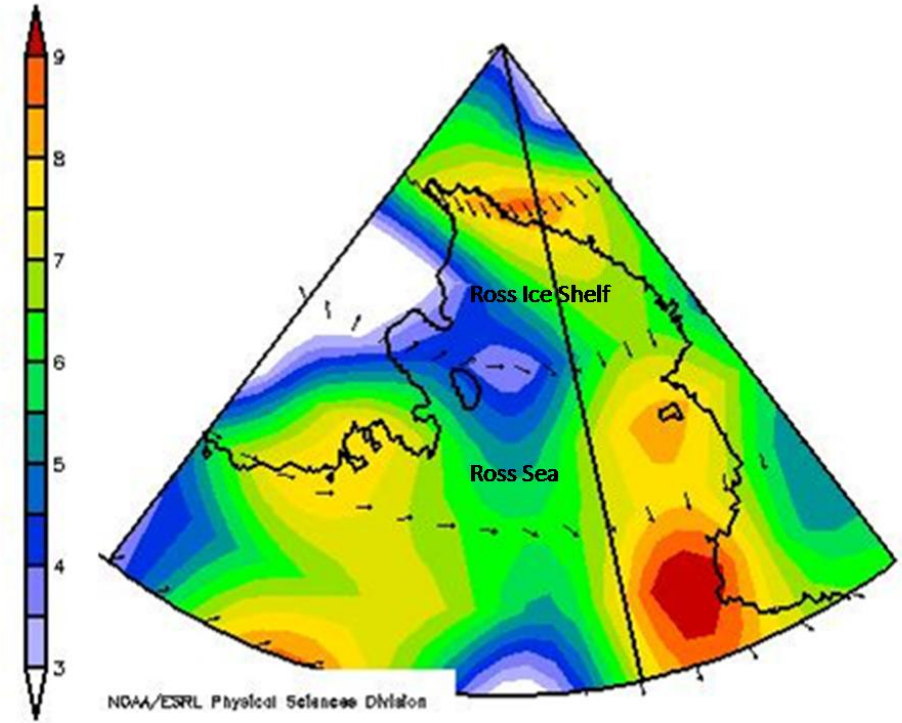

Fig. 12. Reanalysis-Derived Surface Vector Wind Speed (m/s) and Direction for 18–25 January composite period. Image provided by the NOAA/ESRL Physical Sciences Division, Boulder Colorado from their Web site at http://www.esrl.noaa.gov/psd/.

TCD
3, 1069–1107, 2009